Front. Earth Sci. 2025, 19(3): 364–379
https://doi.org/10.1007/s11707-025-1154-1

RESEARCH ARTICLE

Mapping paddy rice in northeast China with a knowledge-based algorithm and time series optical, microwave, and thermal imagery

Chenchen ZHANG[1], Xiangming XIAO (✉)[1], Xinxin WANG[2], Yuanwei QIN[3,1], Russell DOUGHTY[4], Xuebin YANG[5], Cheng MENG[1], Yuan YAO[1], Jinwei DONG[6]

1 School of Biological Sciences, Center for Earth Observation and Modeling, University of Oklahoma, Norman, OK 73019, USA
2 Key Laboratory for Biodiversity Science and Ecological Engineering, National Observations and Research Station for Wetland Ecosystems of the Yangtze Estuary (Ministry of Education), Institute of Biodiversity Science and Institute of Eco-Chongming, School of Life Sciences, Fudan University, Shanghai 200438, China
3 College of Geography and Remote Sensing, Hohai University, Nanjing 211100, China
4 College of Atmospheric and Geographic Sciences, University of Oklahoma, Norman, OK 73019, USA
5 Geography and the Environment Department, Syracuse University, Syracuse, NY 13244, USA
6 Key Laboratory of Land Surface Pattern and Simulation, Institute of Geographic Sciences and Natural Resources Research, Chinese Academy of Sciences, Beijing 100101, China

Abstract Accurate and timely large-scale paddy rice maps with remote sensing are essential for crop monitoring and management and are used for assessing its impacts on food security, water resource management, and transmission of zoonotic infectious diseases. Optical image-based paddy rice mapping studies employed the unique spectral feature during the flooding/transplanting period of paddy rice. However, the lack of high-quality observations during the flooding/transplanting stage caused by rain and clouds and spectral similarity between paddy rice and natural wetlands often introduce errors in paddy rice identification, especially in paddy rice and wetland coexistent areas. In this study, we used a knowledge-based algorithm and time series observation from optical images (Sentinel-2 and Landsat 7/8) and microwave images (Sentinel-1) to address these issues. The final 10-m paddy rice map had user's accuracy, producer's accuracy, F1-score, and overall accuracy of 0.91 ± 0.004, 0.74 ± 0.010, 0.82, and 0.98 ± 0.001 (± value is the standard error), respectively. Over half (62.0%) of the paddy rice pixels had a confidence level of 1 (detected by both optical images and microwave images), while 38.0% had a confidence level of 0.5 (detected by either optical images or microwave images). The estimated paddy rice area in northeast China for 2020 was 60.83 ± 0.86 × 10^3 km^2. Provincial and municipal rice areas in our data set agreed well with other existing paddy rice data sets and the Agricultural Statistical Yearbooks. These findings indicate that knowledge-based paddy rice mapping algorithms and a combination of optical and microwave images hold great potential for timely and frequently accurate paddy rice mapping in large-scale complex landscapes.

Keywords paddy rice, rice-wetland coexistence area, flooding signal, knowledge-based algorithm, confidence map

1 Introduction

Paddy rice plays crucial roles in human food security, water management, disease transmission, and climate change. Paddy filed are related to the transmission of zoonotic diseases, as they assume an important forum for the exchange of avian influenza virus for poultry and waterfowl (Gilbert et al., 2014). Moreover, seasonal flooded paddy fields emits ~34.2 million tons of methane annually, affecting atmospheric chemistry and climate change (Tollefson, 2022). As the most water-intensive crop, an expansion in rice cultivation areas may increase water consumption (Elliott et al., 2014). Therefore, accurate, updated, and spatially fine-resolution maps of paddy rice are urgently needed for informing policy decisions, safeguarding global food and water security, and promoting environmental protection and sustainability.

Received February 14, 2024; accepted February 14, 2025

E-mail: xiangming.xiao@ou.edu

Remote sensing technology provides powerful and efficient tools for paddy rice mapping and monitoring (Dong and Xiao, 2016). In the past decades, numerous studies have produced paddy rice maps at diverse spatial scales using very high spatial resolution (VHSR, meter scale), high spatial resolution (HSR, tens of meters scale), and moderate spatial resolution (MSR, hundreds of meters scale) imagery at local (Huang and Zhang, 2023), national (Singha et al., 2019), and continental scales (Dong et al., 2016a) (Table 1). Paddy rice mapping algorithms can be categorized into four groups: 1) visual interpretation and classification, 2) data-based unsupervised classification, 3) information-based supervised classification, and 4) knowledge-based classification. The information-based supervised classification and knowledge-based classification methods are currently the most extensively used methods (Dong et al., 2015; Singha et al., 2019; You et al., 2021). However, information-based classification requires large amount of high-quality paddy rice training data, and the accuracy of resultant rice maps is heavily reliant upon these training data, making this method difficult to generalize and apply to large regions and other years (You et al., 2021; Huang and Zhang, 2023). Moreover, the complexity and opacity of this method pose challenges in comprehending the rationale behind the model's final decisions (Zhang et al., 2023a).

Knowledge-based paddy rice mapping algorithms rely on the distinctive biophysical feature of paddy fields, that is, rice plants grow in flooded soils, and in the transplanting and early growth stage (open canopy), paddy fields are composed of a mix of green rice plants and surface water, (Xiao et al., 2005a, 2006). The mix of rice plant and surface water in the transplanting and early growth stage (open canopy) can be detected through a water-related vegetation index (Land Surface Water Index, LSWI) and greenness-related vegetation indices (Normalized Difference Vegetation Index, NDVI; Enhanced Vegetation Index, EVI), as evidenced by the unique spectral feature (trait) of water-related vegetation index (LSWI) being larger than greenness-related vegetation indices (NDVI, EVI). During the flooding/transplanting stage, the image pixels with LSWI > EVI or LSWI > NDVI were identified as paddy rice (Xiao et al., 2005, 2006). This knowledge of paddy rice has been effectively employed in mapping paddy rice in south China (Xiao et al., 2002a, 2005a), northeast China (Zhang et al., 2015; Dong et al., 2016a), Northeast Asia (Dong et al., 2016a), monsoon Asia (Zhang et al., 2020), and South and Southeast Asia (Xiao et al., 2006). However, application of the knowledge-based algorithm to those areas with both paddy rice and natural wetlands needs to pay more attention in time series data analyses, as natural wetlands (e.g., marsh, swamp) have a similar stage of mixed green plants and surface water (open canopy) during their growing season, which may lead to commission errors in paddy rice identification (Zhou et al., 2016; Huang and Zhang, 2023). To tackle this issue, maps of natural wetlands are then used as the mask layer to reduce the commission error (Zhang et al., 2015). In addition, clouds and shadows could reduce the amount of good-quality optical observations during the rice flooding/transplanting period (Gómez et al., 2016), leading to omission errors in paddy rice classification.

Synthetic aperture radar (SAR) has a sensitivity to surface water and flooded vegetation (McNairn et al., 2018; Li et al., 2020), and thus has the potential to provide complementary information to optical imagery, which may solve the problem of confusion between paddy rice and wetlands when only optical images are used in land cover classification. Sentinel-1 A/B data have been freely available since 2014, and its 'all-weather', 'all-day' data collection capability with a 12-day revisit period (6-day when A/B images are combined) can generate dense time series SAR images, allowing for tracking seasonal dynamics of paddy rice and wetlands at

Table 1 A sample list of publications on image data sources and algorithms for paddy rice mapping

Methods	Optical			SAR (RADARSAT, ERS-1, Sentinel-1)	Optical + SAR (Landsat, SPOT, RADARSAT, Sentinel-2, Sentinel-1)
	VHSR (<10-m; e.g., QuickBird, IKONOS, UAV)	HSR (10-m–30-m; e.g., Sentinel-2, SPOT, Landsat)	MSR (250-m–500-m; e.g., MODIS)		
Visual interpretation and classification	(Liu et al., 2017)	(Rao and Rao, 1987)			
Data-based unsupervised classification (e.g., K-means, ISODATA)	(Turker and Ozdarici, 2011)	(Nguyen et al., 2012; Pan et al., 2010)	(Gumma et al., 2011)	(Parmuchi et al., 2002)	
Information-based supervised classification (e.g., MLC, NN, DT, SVM, RF, ETUnet)	(Yan et al., 2023)	(Huang et al., 2020; Ni et al., 2021; Panigrahy and Parihar, 1992; You et al., 2021)	(Guan et al., 2016; Guan et al., 2018)	(Le Toan et al., 1997; Shao et al., 2001; Singha et al., 2019)	(Huang and Zhang, 2023; Oguro et al., 2001)
Knowledge-based classification		(Dong et al., 2015; Dong et al., 2016a; Qin et al., 2015b; Zhou et al., 2016)	(Xiao et al., 2006; Xiao et al., 2005a; Zhang et al., 2015)	(Li et al., 2020)	**This study**

Notes: UAV: Unmanned aerial vehicle; MLC: Maximum likelihood classifier; NN: Neural Networks; DT: Decision tree; SVM: Support vector machine; RF: Random Forest; ETUnet: Enhanced-TransUnet.

various growth stages (Geudtner et al., 2014). Before the transplanting of rice seedlings, paddy fields are inundated with open surface water from irrigation (flooding stage) (Xiao et al., 2005a). During the subsequent transplanting stage, rice fields become a mix of rice seedlings and water. In contrast, wetlands only experience a stage of a mixture of surface water, dead and newly emerging plants, and soils in the period from snowmelt to canopy closure. Distinct water-related surface structures (presence or absence of plants during the flooding stage) between paddy rice and wetlands lead to different scattering processes, which cause discrepancies in SAR backscatter signals, and thus may serve as the key to distinguishing between paddy rice and wetlands using SAR images (Brisco et al., 2009; Brisco, 2015). However, our understanding of the backscatter characteristics of C-band Sentinel-1 data in paddy rice and wetlands is limited, and the potential of time-series Sentinel-1 imagery for differentiating between these two land covers has not yet been evaluated.

As the world's leading rice producer, China accounts for ~28% of global rice production (FAOSTAT, 2020). In China, the rapid extension of rice cultivation in the northeast in the last few decades and the consequent increase in grain production have led to a shift in the center of crop production to the northeast (Dong et al., 2016b). As per the National Bureau of Statistics, the rice cultivated area in northeast China was ~5.4 million ha (54×10^3 km^2) with a yield of ~4.1×10^7 tons in 2020, accounting for ~18% of the country's rice cultivation area and ~20% of its yield. Notably, northeast China has highly concentrated and diverse wetlands, with 15 sites listed as internationally important wetlands. The extensive distribution of wetlands and paddy rice in northeast China poses a great challenge to paddy rice extraction.

The objectives are to (i) develop an improved knowledge-based paddy rice mapping algorithm by integrating microwave (Sentinel-1 A/B, S1), optical (Sentinel-2 A/B, S2; Landsat, LS), and thermal (MODIS) time series images; (ii) explore the potential of S1 polarization band to identify paddy rice; and (iii) generate paddy rice maps with a high accuracy and known confidence levels (1 for detection by both optical images and microwave images, 0.5 for detection by either optical images or microwave images).

2 Materials and methods

2.1 Study area

Northeast China includes the provinces of Liaoning, Jilin, Heilongjiang, and four municipalities in the eastern part of Inner Mongolia Autonomous Region (Fig. 1). This area features a cold temperate and humid/sub-humid climate, with annual accumulative air temperatures higher than 0°C on 2000°C·day–4200°C·day and higher than 10°C on 1600°C·day–3600°C·day. Frost-free period is typically 140 to 170 days (Dong et al., 2016a). Annual precipitation averages between 500 and 800 mm, with the majority occurring in July and August. Due to temperature constraints, only single-season crops are cultivated in this region.

2.2 Data sets

2.2.1 Sentinel-2 data

We used S2A/B surface reflectance (SR) data from January 1, 2020, to December 31, 2020, in Google Earth

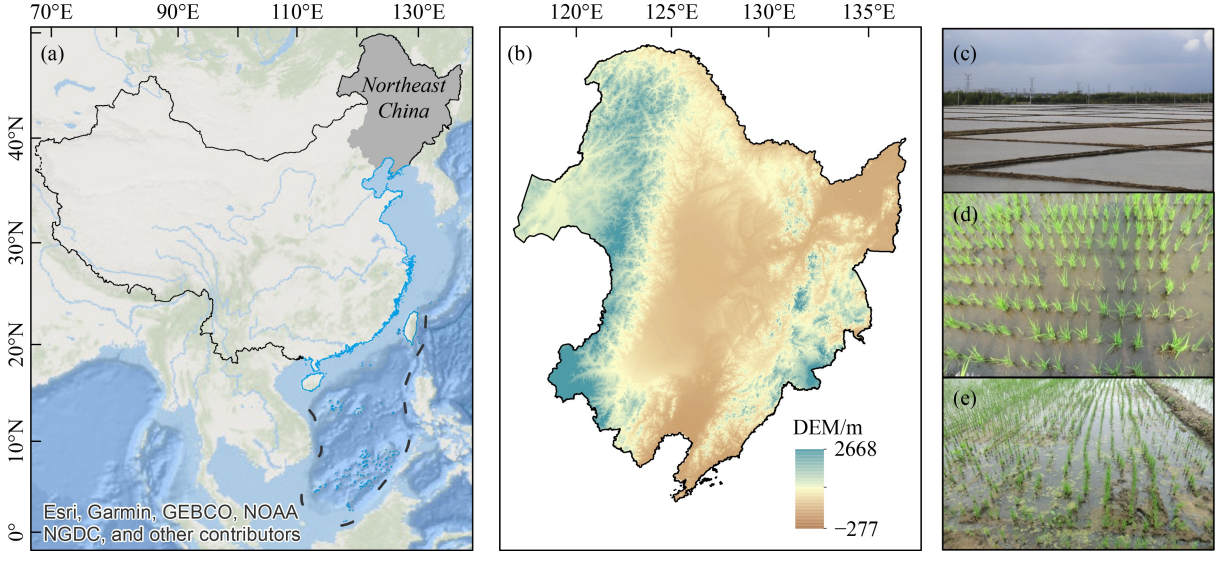

Fig. 1 (a) Location and (b) terrain of northeast China. (c–e) Field photos of paddy rice at the (c) flooding and (d, e) transplanting phases. Field photos were downloaded from the CEOM Global Geo-Referenced Field Photo Library.

Engine (GEE) (Fig. 2(a)), and removed bad-quality observations associated with clouds by using the Cloud Probability (MSK_CLDPRB) band. Cloud shadows and cirrus were also eliminated with Scene Classification (SCL) band. Snow/ice observations were removed by the Snow Probability (MSK_SNWPRB) band and the criteria of Normalized Difference Snow Index (NDSI) > 0.4 and Near-infrared (NIR) > 0.11 (Hall et al., 1995).

Two greenness-related vegetation indices, NDVI (Tucker, 1979) and EVI (Huete et al., 1997; Huete et al., 2002), and a water-related spectral index, LSWI (Xiao et al., 2004, 2005b), were calculated for each S2 image with Eqs. (1)–(3). NDVI and EVI are used for monitoring and detecting vegetation, and LSWI is used for detecting vegetation and soil water:

$$\mathrm{NDVI} = \frac{\mathrm{NIR} - \mathrm{Red}}{\mathrm{NIR} + \mathrm{Red}}, \tag{1}$$

$$\mathrm{EVI} = 2.5 \times \frac{\mathrm{NIR} - \mathrm{Red}}{\mathrm{NIR} + 6\mathrm{Red} - 7.5\mathrm{Blue} + 1}, \tag{2}$$

$$\mathrm{LSWI} = \frac{\mathrm{NIR} - \mathrm{SWIR}}{\mathrm{NIR} + \mathrm{SWIR}}, \tag{3}$$

where Blue, Red, NIR, and SWIR are SR values for blue, red, near-infrared, and shortwave-infrared bands.

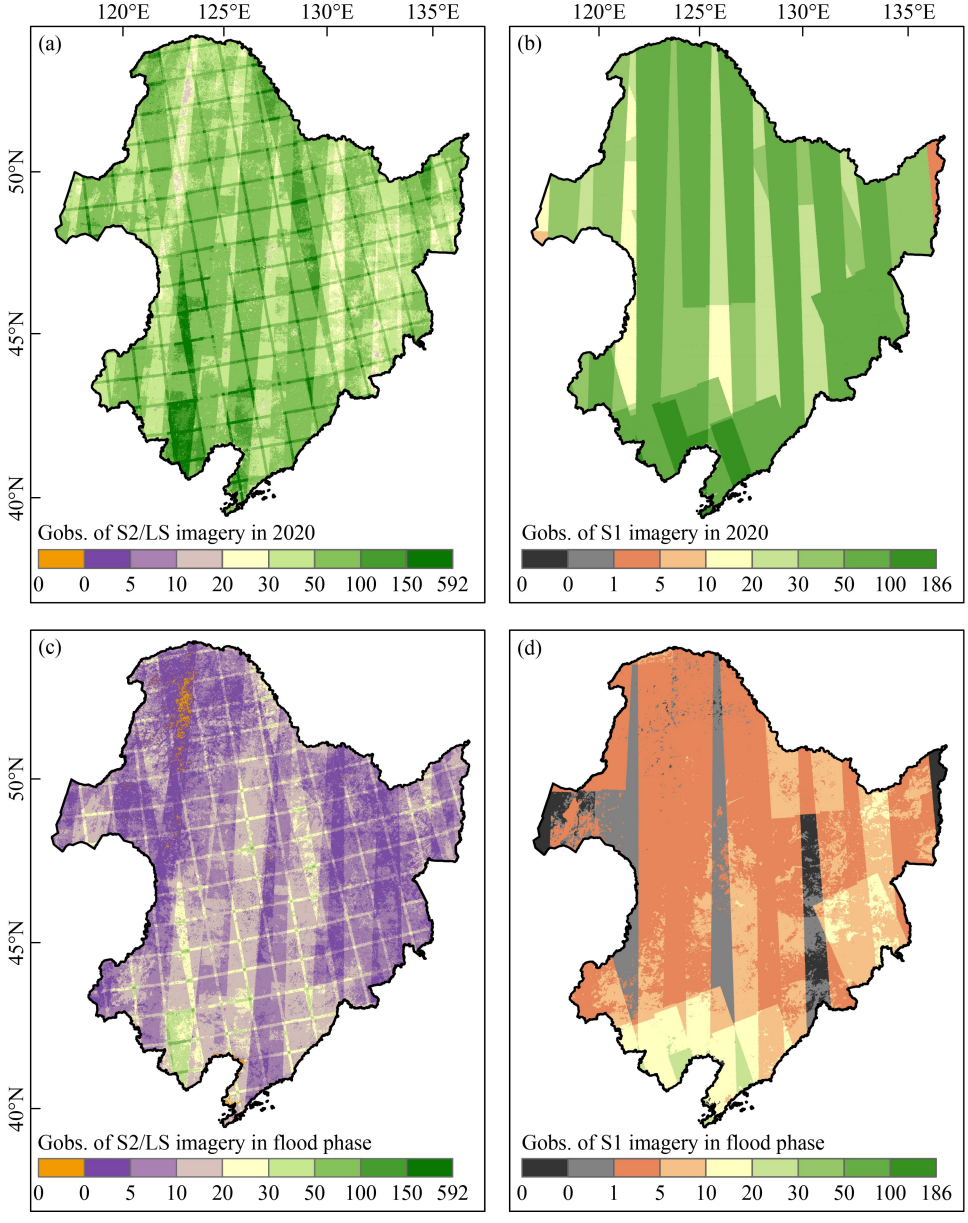

Fig. 2 (a–b), Good-quality observations (Gobs.) of Sentinel-2/Landsat imagery in (a) the whole year and (b) the flooding phase (start of the thermal growing season of > 5°C to the end of June, TGS-5-S ~ DOY 181d) in 2020. (c–d), Total observations of Sentinel-1 images in the (c) whole year and (d) the flooding phase in 2020. TGS-5-S and DOY 181d are the start (SOF) and end (EOF) of the flooding phase, respectively, and the reasons for setting these thresholds are described in Section 2.3.1.

2.2.2 Landsat data

We acquired LS 7/8 SR data from January 1, 2020, to December 31, 2020, in GEE (Fig. 2(a)), and removed clouds, cloud shadows, and cirrus observations using the BQA bitmask band. Snow/ice observations were removed by (NIR > 0.11 and NDSI > 0.4) (Hall et al., 1995). NDVI, EVI, and LSWI were calculated for each LS image using Eqs. (1)–(3). For spatial consistency with S2 imagery, these vegetation index collections were re-sampled to 10-m spatial resolution by the nearest neighbor method. LS data were integrated with S2 data to increase the availability of high-quality optical observations.

2.2.3 Sentinel-1 data

The C-band (~5.5 cm) S1A/B Level 1 Ground Range Detected (GRD) product in the Interferometric Wide (IW) swath model from January 1, 2020, to December 31, 2020, was also collected in GEE (Fig. 2(c)). S1 imagery provides dual-polarized data in the VV and VH bands (Torres et al., 2012). Calibrated and ortho-corrected S1 imagery in GEE were generated by using the Sentinel-1 Toolbox, which includes thermal noise removal, radiometric calibration, and terrain correction. Final terrain-corrected values were converted to decibel (dB) by 10log10 (DN). S1 data were combined to provide complementary information to optical imagery and to explore its capability of identifying paddy rice from wetlands.

2.2.4 MODIS data

The 8-day nighttime land surface temperature (nLST) data from MYD11A2 for 2020 were collected in GEE. DN values from MYD11A2 were transformed to centigrade unit values using LST (°C) = DN × 0.02–273.15 (Wan, 2008). Linear interpolation was applied to fill in the missing data using data from adjacent times before and after the missing values (Liu et al., 2020). Temperature is a primary constraint on plant growth and crop cultivation in the cold temperate zones. Prior studies have used air temperature or land surface temperature to simulate the thermal growing season (TGS) (Dong et al., 2015, 2016a; Zhang et al., 2015, 2020). Compared to air temperature data measured at 2 m above the ground and simulated from multiple sources, the MODIS nLST data set is more relevant for capturing temperature constraints on rice seedlings due to its measuring height, higher spatial resolution, and lower uncertainties. We utilized MODIS nLST to define the start of the thermal growing season (phenology timing) by an nLST threshold of > 5°C (TGS-5), i.e., the start of TGS-5 (TGS-5-S), which was used to delineate the period in a year for data analyses.

2.3 Knowledge-based paddy rice mapping algorithm

We proposed an enhanced knowledge-based algorithm to delineate paddy rice (Fig. 3). First, we generated a potential cropland layer by removing non-cropland types using our existing maps of specific land cover types. Then, within the cropland layer, we combined S2/LS, S1, and MODIS nLST data to identify paddy rice.

2.3.1 Phenology analysis of paddy rice

Paddy rice and wetlands are the only two vegetation types with a period of flooding (open water or a mix of water and plants/soils). In general, paddy fields go through several stages: 1) bare soil, 2) flooding (open surface water), 3) rice seedlings transplanting, 4) seedling growth (open canopy), and 5) canopy closed, as illustrated by time series vegetation index data from one pixel in 2020 (Fig. 4(a)). During the bare soil stage, paddy fields lack green crops and have low soil moisture, NDVI and EVI values are low, and LSWI values are negative. As farmers irrigate the field (flooding stage), paddy fields are covered with open surface water, and LSWI rises

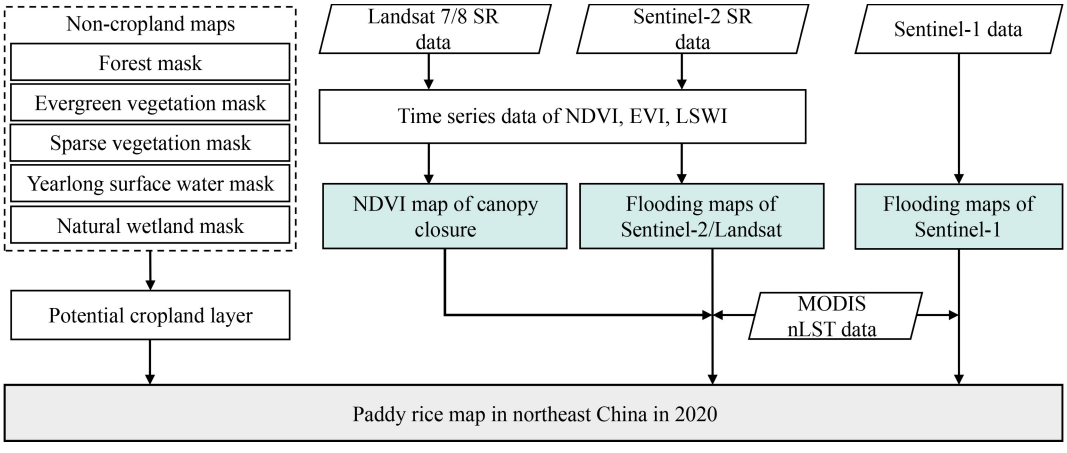

Fig. 3 Flowchart of identifying paddy rice.

substantially while NDVI and EVI remain at low values. At the rice transplanting stage, paddy fields become a mix of water and rice plants, and NDVI and EVI rise but are still lower than LSWI. This flooding/transplanting transition can be identified by LSWI > EVI or LSWI > NDVI, indicating that water-related vegetation indices exceed greenness-related vegetation indices (Xiao et al., 2002b, 2005a, 2006). This relationship between LSWI and NDVI/EVI was also observed from the data in 2018 and 2019 (Fig. S1), and was reported by previous studies in various regions and years, for example, northeast China from 1986 to 2010 (Dong et al., 2015), south China in 2002 (Xiao et al., 2005a) and 2013 (Wang et al., 2015), China and India from 2000 to 2015 (Zhang et al., 2017), Northeast Asia from 2000 to 2014 (Dong et al., 2016a, b), and South and South-east Asia in 2002 (Xiao et al., 2006). As rice seedlings grow, NDVI and EVI gradually increase until the canopy is closed, at which time NDVI and EVI values are higher than the LSWI value again (Fig. 4(a)).

To avoid damage to rice seedlings from low temperatures, rice fields are irrigated or flooded and rice seedlings are transplanted when the stable air temperature threshold (~5°C) is reached (Zhang et al., 2015), so we defined the start of flooding (SOF) temporal window when the nLST remains above 5°C (TGS-5-S). Based on the rice crop calendar and climate data (Zhang et al., 2015; Dong et al., 2016a), by the end of June (DOY 181d), the temperate zone begins to enter the peak growing season and rice seedlings have been transplanted into the field, so we identified DOY 181d as the end of flooding (EOF) temporal window.

Wetlands (e.g., marsh) show a similar relationship between LSWI and NDVI/EVI (LSWI > EVI or LSWI > NDVI) in the early growing season with a mix of open water and dead/newly emerging plants and soils) (Fig. 4(b)), which aligns with the rice transplanting stage. However, during the rice flooding stage, LSWI values are notably higher due to the complete coverage of open surface water, in contrast to the relatively lower water percentage in wetland pixels due to dead plants (Figs. 4(a) and 4(b)). This discrepancy can be attributed to LSWI's ability to represent the proportion of water bodies within each pixel (Chandrasekar et al., 2010). To assess the generalizability of the individual pixel analyses, we analyzed the LSWI values of the paddy rice samples (24,831 pixels) at the flooding/transplanting stage when LSWI > NDVI or LSWI > EVI, and the results showed that 95.9% of paddy rice pixels had LSWI > 0.3 (Fig. 5(a)). Thus, we introduced an additional constraint (LSWI > 0.3) to the flooding signal identification algorithm (Eq. (4)) to depict the unique 'open water' stage of paddy rice (Fig. 4(a)). This adjustment serves to minimize the interference of other flooded lands in paddy rice identification:

$$\mathrm{Flood}_{\mathrm{opt}}(t) = \begin{cases} 1, & [(\mathrm{LSWI}_t > \mathrm{NDVI}_t \text{ or } \mathrm{LSWI}_t > \mathrm{EVI}_t) \text{ and } (\mathrm{LSWI}_t > 0.3)] \\ 0, & \text{Others} \end{cases} \quad (\mathrm{SOF} < t < \mathrm{EOF}), \tag{4}$$

where $\mathrm{Flood}_{\mathrm{opt}}(t)$ is the status of flooding, with 1 indicating the presence of a flooding signal at time t, and 0 indicating the absence of a flooding signal at time t. The start (SOF) and end (EOF) of the flooding phase are TGS-5-S and DOY 181d, respectively, and t is the time at which the observation is acquired.

SAR backscatter observations are sensitive to vegetation structure and hydrologic conditions, causing different backscatter energy levels during various growth stages in paddy rice and wetlands. At the bare soil stage of paddy rice, S1 C-band microwave signals reach the rough ground surface and primarily undergo diffuse scattering. During the subsequent flooding stage, the

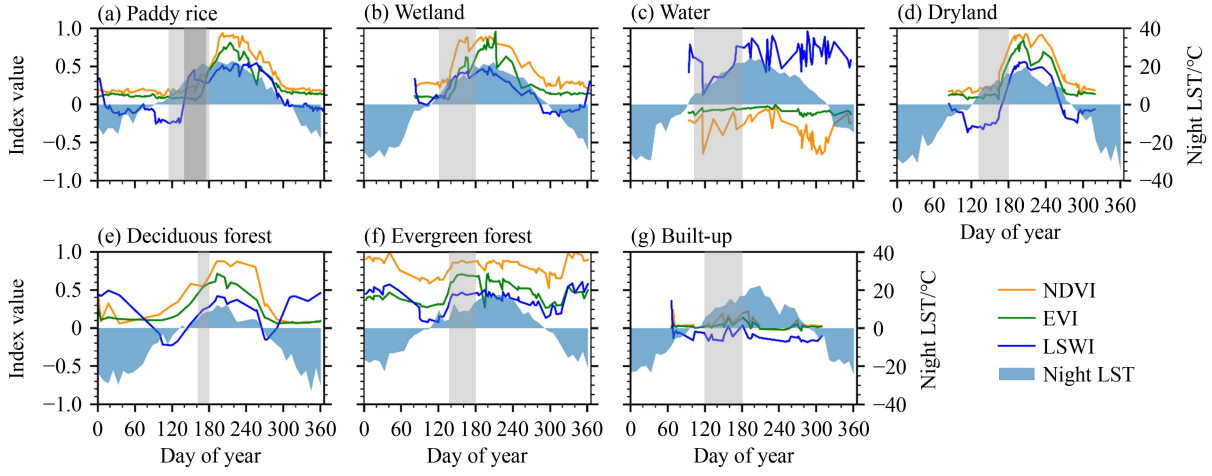

Fig. 4 Time series NDVI, EVI, LSWI, and nLST for paddy rice and other major land covers. These time series profiles were generated using one sample point (one pure pixel) for each land cover. Light gray semitransparent boxes present the time window (TGS-5-S−DOY 181d) used for paddy rice identification. The dark gray semitransparent box in (a) presents the paddy rice flooding stage.

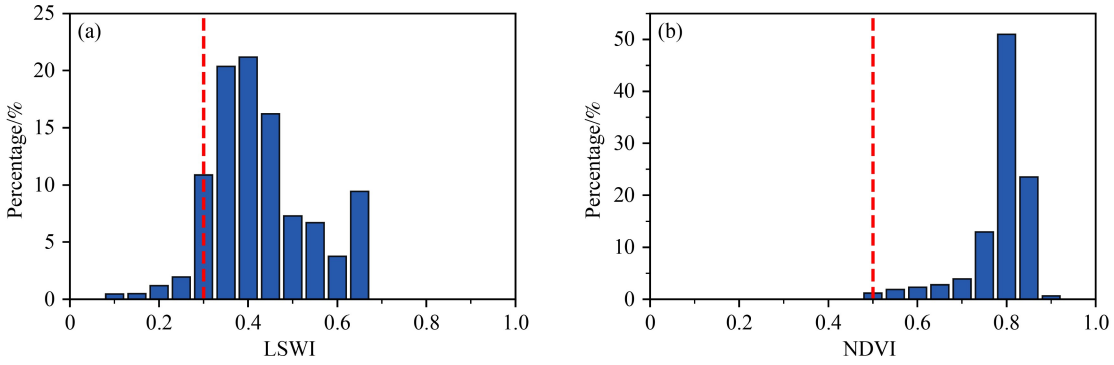

Fig. 5 The histograms of (a) LSWI values in the flooding/transplanting stage when LSWI > NDVI or LSWI > EVI and (b) NDVI values at the closed-canopy stage of paddy rice.

scattering is specular or mirror-like and little energy is returned to the sensor, leading to a rapid drop in backscatter energy to less than −14 dB of VV and −24 dB of VH (Fig. 6(a)) (Brisco, 2015). On the contrary, during the flooding stage of wetlands, the mixture of open water, dead plants, and soils results in double-bounce scattering and volume scattering, causing enhanced VV and VH backscattering that well exceeds the value observed for open water (Brisco, 2015) (Fig. 6(b)). In other words, only paddy rice has obvious decreasing trends at both VV and VH during the flooding stage. Given the significant disparity in VV trends between paddy rice and natural wetlands, we employed VV to detect flooding signals in paddy rice using Eq. (5). We then checked the VV time series of 24,831 rice pixels, of which 93.3% conformed to Eq. (5), which was consistent with the single-pixel time series analysis in Fig. 6:

$$\mathrm{Flood_{SAR}}(t) = \begin{cases} 1, & (\mathrm{VV}_t < \mathrm{VV}_{t-1} \text{ and } \mathrm{VV_t} < -14) \\ 0, & \text{Others} \end{cases} \quad (\mathrm{SOF} < t < \mathrm{EOF}), \tag{5}$$

where $\mathrm{Flood_{SAR}}(t)$ is the status of flooding, with 1 indicating the presence of a flooding signal at time t, and 0 indicating the absence of a flooding signal at time t. SOF and EOF are TGS-5-S and DOY 181d, respectively, and t is the time at which the observation is acquired.

NDVI is highly correlated to the leaf area index (LAI) of rice. Rice grows quickly after transplanting and LAI typically reaches its peak within two months (Xiao et al., 2002b). Therefore, to avoid the effect of continuous flooded pixels on the resultant paddy rice map, NDVI of the canopy closure stage ($\mathrm{NDVI_{closed\text{-}canopy}}$) was calculated, and 100% of the paddy rice pixels had $\mathrm{NDVI_{closed\text{-}canopy}} > 0.5$ (Fig. 5(b)). The onset timing of canopy closure was defined as the date two months (60 d) after the last detected flooding/transplanting signal (Fig. 4(b)) (Xiao et al., 2002b).

2.3.2 Algorithm for identifying paddy rice

We utilized the unique feature of paddy rice being covered by open water during the flooding/transplanting stage to delineate paddy rice from other land covers. Time series S2/LS optical images ($\mathrm{Flood_{opt}}(t)$) and S1 SAR images ($\mathrm{Flood_{SAR}}(t)$) were combined to identify open water during the flooding stage. Times series S2/LS

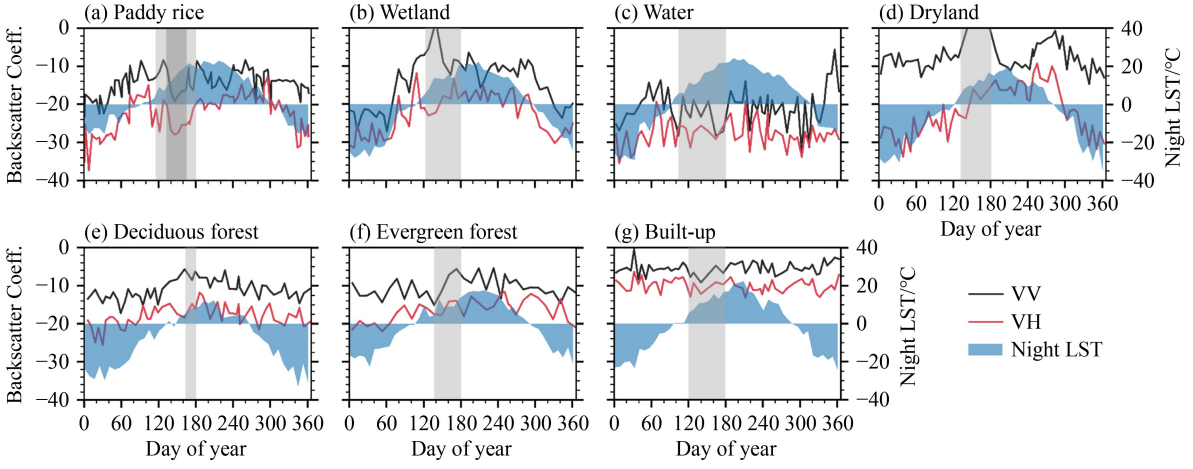

Fig. 6 Time series VV, VH, and nLST for paddy rice and other major land covers. Light gray semitransparent boxes present the time window used for paddy rice identification. Dark gray semitransparent box in (a) presents the paddy rice flooding stage.

images ($NDVI_{closed\text{-}canopy}$) were also employed to verify vegetation presence after canopy closure. We divided the paddy rice identification into three cases based on the availability of optical (N_{opt}) and SAR (N_{SAR}) images during the flooding stage, i.e., 1) both S2/LS and S1 data were available ($N_{opt} > 0$ and $N_{SAR} > 1$), 2) only S2/LS data were available ($N_{opt} > 0$ and $N_{SAR} \leqslant 1$), and 3) only S1 data were available ($N_{opt} = 0$ and $N_{SAR} > 1$). In summary, pixels meeting the criteria described in Eq. (6) were classified as paddy rice:

$$\text{Paddy rice} = \begin{cases} NF_{opt} \geqslant 1,\ NF_{SAR} \geqslant 1, \text{ and } NDVI_{closed-canopy} \geqslant 0.5, & N_{opt} > 0 \text{ and } N_{SAR} > 1 \\ NF_{opt} \geqslant 1 \text{ and } NDVI_{closed-canopy} \geqslant 0.5x, & N_{opt} > 0 \text{ and } N_{SAR} \leqslant 1 \\ NF_{SAR} \geqslant 1 \text{ and } NDVI_{closed-canopy} \geqslant 0.5, & N_{opt} = 0 \text{ and } N_{SAR} > 1 \end{cases}, \quad (6)$$

where NF_{opt} and NF_{SAR} are the number of flooding signals detected in optical (S2/LS) and SAR (S1) images at the flooding stage, respectively. N_{opt} and N_{SAR} are the number of good-quality optical images and the number of SAR images during the flooding phase, respectively.

2.3.3 Generation of paddy rice map

We first generated a potential map of cropland layer and non-cropland layer in northeast China by using several available non-cropland layers data sets in 2020. These non-cropland layers data products were produced by applying or modifying the knowledge-based algorithms reported in our previous publications, including yearlong surface water (Zou et al., 2018; Wang et al., 2020a), evergreen vegetation (Dong et al., 2015; Wang et al., 2020b; Zhang et al., 2024), forest (Qin et al., 2015a; Qin et al., 2016; Qin et al., 2021), sparse vegetation (Zhang et al., 2015; Qin et al., 2017), and natural wetlands (Zhang et al., 2024). These non-cropland layer data products were documented with high accuracy in our previous publication (Zhang et al., 2024) and were used in this study. For the pixels labeled as the potential cropland layer, paddy rice can be identified using Eq. (6).

2.3.4 Confidence levels of paddy rice pixels identified by image analyses

The resultant paddy rice map can be assigned different confidence levels (1 and 0.5) based on the detection of flooding signals from both optical and SAR imagery in the same time period (within 5 days), as irrigation and flooding events are continuous. Using the S2/LS flooding time series as a reference, on date t, the confidence level of the paddy rice pixel was designated as 1 if flooding was detected by both optical S2/LS images and microwave S1 images within 5 days before or after date t ($t \pm 5$ days). If flooding was detected only by optical images or microwave images within 5 days, the confidence level was set to 0.5 (Eq. (7)). The final confidence level for paddy rice was determined using the maximum value from the confidence time series:

$$\text{Confidence}(t) = \begin{cases} 1, & Flood_{opt}(t) = 1 \text{ and } Flood_{SAR}(t \pm 5) = 1 \\ 0.5, & \text{Others} \end{cases}, \quad (7)$$

where $\text{Confidence}(t)$ is the confidence level of the identified paddy rice pixel at date t, $Flood_{opt}(t)$ is flooding status (0 or 1) detected by S2/LS images at date t, and $Flood_{opt}(t \pm 5)$ is the flooding status (0 or 1) detected by S1 images within 5 days before and after date t.

2.4 Paddy rice map assessment and inter-comparisons with other data sets

Stratified random sampling method was used to collect validation samples, by integrating GPS-based field photos, Google Earth VHSR images, and S2 images in 2020. First, we obtained the 2020 national land cover map from China's National Land Use and Cover Change data set, which includes paddy rice as one of land cover types (Liu et al., 2014). This map served as the base map for dividing northeast China in six layers: paddy rice, wetlands, surface water, forest and other natural vegetation, upland crops, and built-up and barren lands. Second, random points and their square buffers of 60-m by 60-m were generated within each stratum. This 60-m distance was to match LS and S1/2 spatial resolutions and paddy field size. Third, each buffer was visually examined using Google Earth VHSR images and S2 images in 2020. Four S2 median composites from early Mar. to early Apr., mid-Apr. to mid-Jun., early Jul. to late Aug., and late Sept. to late Oct., corresponding to bare soil, flooding/transplanting, growing, and harvest stages of rice, respectively (Dong et al., 2015; Ni et al., 2021), were used to accurately recognize paddy rice. Field photos with coordinates (Fig. 7(a)) were used as auxiliary data to check each land cover type. Buffers without explicit land cover information were excluded. In total, 114 samples (5317 pixels) for paddy rice and 461 samples (26553 pixels) for non-paddy rice were collected. The non-paddy rice category included 64 samples (6284 pixels) for wetlands, 108 samples (5010 pixels) for upland crops, 213 samples (11306 pixels) for forest and other natural vegetation, 28 samples (1525 pixels) for surface water, and 48 samples (2428 pixels) for built-up and barren lands (Fig. 7(c)). These validation samples were used to generate a confusion matrix to evaluate the accuracy of the resulting paddy rice map with difference confidence levels. As recommended by good practice for accuracy assessment and area estimation (Olofsson et al., 2014), we then adjusted the accuracy and area by considering paddy rice and non-paddy rice areas.

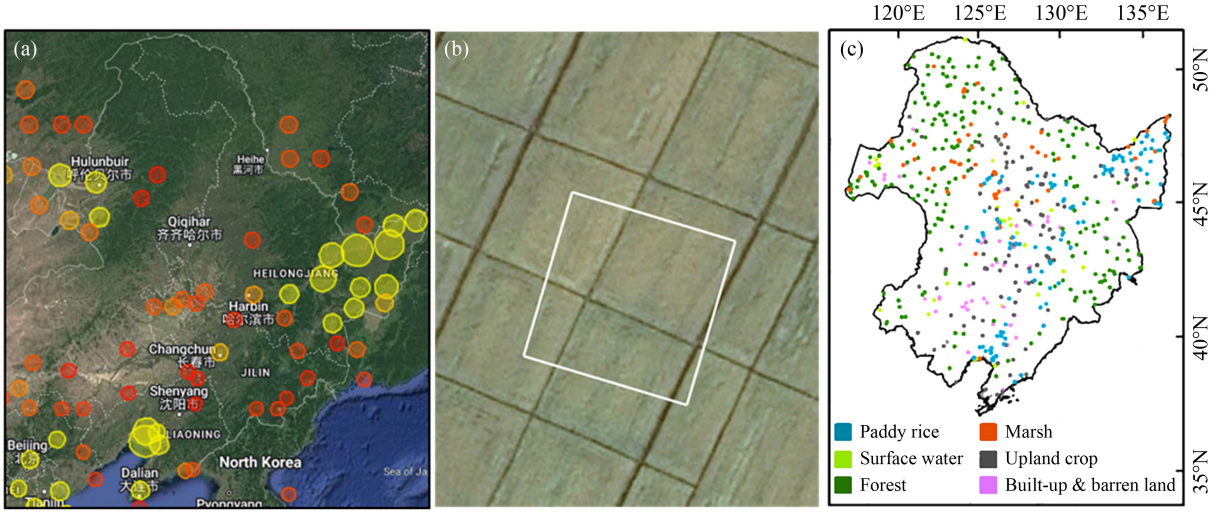

Fig. 7 Generation of validated regions of interest (ROIs). (a) Spatial distribution of field photos from Global Field Photo Library (accessed on October 4, 2023); circle sizes represent the photo intensity; (b) An example of a square ROI of 60-m by 60-m; (c) Spatial distribution of validation samples.

We collected data on rice planting areas in 2020 from provincial and municipal Statistical Yearbooks published in 2021, which provided statistics for the previous years. In addition, You et al. (2021) generated a paddy rice map using time series S2 imagery and the random forest algorithm for 2019. We overlaid the validation samples with the paddy rice map from You et al.'s (2021) study to calculate its accuracies and compare them with those from this study. We also conducted a comparison of the rice area calculated from the resultant map and error-adjusted paddy rice area with Statistical Yearbooks and You et al.'s (2021) study at the regional, provincial, and municipal levels using paddy rice areas derived from our map. Municipal comparisons were conducted using the linear regression and metrics including mean error (ME) and root mean square error (RMSE).

3 Results

3.1 Accuracy assessment for paddy rice map

The resulting paddy rice map had a high accuracy with an overall accuracy (OA) of 0.973 (Table 2). The paddy rice category had a user's accuracy (UA) of 0.91, a producer's accuracy (PA) of 0.93, and an F1-score (F1) of 0.92, and the non-paddy rice category had a UA of 0.99, a PA of 0.98, and an F1 of 0.98, respectively. After error adjustment, the paddy rice map achieved an error-adjusted OA (eaOA) of 0.98 ± 0.001. Paddy rice had an error-adjusted UA (eaUA) of 0.91 ± 0.004, an error-adjusted PA (eaPA) of 0.74 ± 0.010, and an error-adjusted F1-score (eaF1) of 0.82. Non-paddy rice had an eaUA of 0.99 ± 0.001, an eaPA of 1.0 ± 0.0002, and an eaF1 of 0.99. Discrepancies between pixel-based and error-adjusted accuracies can be explained by different estimation weights related to areas of each category. We also evaluated the accuracy of each confidence layer. The UA of the paddy rice layer with a confidence level of 1 was 0.94, significantly higher than the UA of the paddy rice layer with a confidence level of 0.5, which was 0.82. The difference in UA between confidence levels suggests the necessity and advantage of integrating the optical and SAR data sets.

3.2 Area and spatial distribution of paddy rice

There was a total 49.61 × 10^3 km^2 of mapped paddy rice in northeast China in 2020, covering ~4.0% of the region's total land area (Table 2). After error adjustment, the total paddy rice area increased to 60.83 × 10^3 km^2 with a standard error of 0.86 × 10^3 km^2, covering ~4.9% of northeast China.

Heilongjiang Province had the largest paddy rice area,

Table 2 A summary for the estimates of accuracies and area for the paddy rice map in 2020. User's accuracy (UA), producer's accuracy (PA), overall accuracy (OA), and F1-score (F1) were calculated from the pixel-based confusion matrix. Error-adjusted user's (eaUA), producer's (eaPA), and overall (eaOA) accuracies and F1-score (eaF1) were calculated from the confusion matrix following the best practice method (Olofsson et al., 2014). This table also shows the paddy rice area (Area, 10^3 km^2) estimated from the resultant map and error-adjusted area (eaArea, 10^3 km^2). SE: standard error

Class	UA	PA	F1	OA	Area	eaUA (SE)	eaPA (SE)	eaF1	eaOA (SE)	eaArea (SE)
Paddy rice	0.91	0.93	0.92	0.97	49.61	0.91 (0.004)	0.74 (0.010)	0.82	0.98 (0.001)	60.83 (0.86)
Non-paddy rice	0.99	0.98	0.98			0.99 (0.001)	1.0 (0.0002)	0.99		

followed by Jilin, Liaoning, and Inner Mongolia (Table 3). Extensive paddy rice was found in plains with flat terrain and abundant water resources (e.g., the Sanjiang Plain and the Songnen Plain). In these plains, paddy rice was mainly cultivated along rivers (Fig. 8 p1−p2). Additionally, paddy rice was sporadically distributed in small patches in mountainous areas near reservoirs (Fig. 8 p3).

Among the detected paddy rice pixels (7.12×10^8), 82.1% were detected by a combination of S2/LS and S1, 17.6% by S2/LS only, and 0.3% by S1 only (Fig. 8). Over half (62.0%) of the paddy rice pixels had a confidence level of 1, indicating that the flooding signals detected by the optical and SAR images did not differ by longer than 5 days (Fig.9). Among these, 2.33×10^3 km^2 (3.32×10^7 pixels, 4.7% of the total paddy rice pixels) had flooding signals detected on the same date by both optical and SAR imagery. 38.0% of the paddy rice pixels had a confidence level of 0.5.

3.3 Inter-comparison to other paddy rice data sets

The accuracy assessment showed that our paddy rice map had similar PA (ours v.s. You et al.'s, 0.93 vs 0.92), UA (0.91 vs 0.92), F1-score (0.92 vs 0.92), and OA (0.97 vs 0.97) with those from You et al.'s (2021) paddy rice map. The total rice area in northeast China in 2020 estimated by our resultant map (49.61×10^3 km^2) was 7.8% lower than that reported in Statistical Yearbooks (53.82×10^3 km^2) and 13.2% lower than the study by You et al., (2021) (57.13×10^3 km^2), respectively (Table 2). The error-adjusted area of paddy rice was 13.0% and 6.5% higher than Statistical Yearbooks and the area reported by You et al., (2021).

At the provincial level, paddy rice areas in our data sets showed high agreement with the areas from You et al.'s (2021) study and Statistical Yearbooks (Fig. 10(a)). However, we detected less paddy rice in Heilongjiang Province, mainly due to the limited observation of S1

Table 3 Paddy rice area (10^3 km^2) in each province of northeast China in 2020

Province	Sentinel-2/Landsat and Sentinel-1 available		Only Sentinel-2/ Landsat available	Only Sentinel-1 available	Confidence summary		Total paddy rice area
	Confidence =1	Confidence =0.5	Confidence =0.5	Confidence =0.5	Confidence =1	Confidence =0.5	
Heilongjiang	22.18	5.76	6.37	0.03	22.18	12.16	34.34
Jilin	3.63	2.28	1.3	0.03	3.63	3.61	7.24
Liaoning	4.18	1.4	0.27	0	4.18	1.67	5.85
Inner Mongolia	0.82	0.59	0.73	0.04	0.82	1.36	2.18
Total	30.81	10.03	8.67	0.1	30.81	18.8	49.61

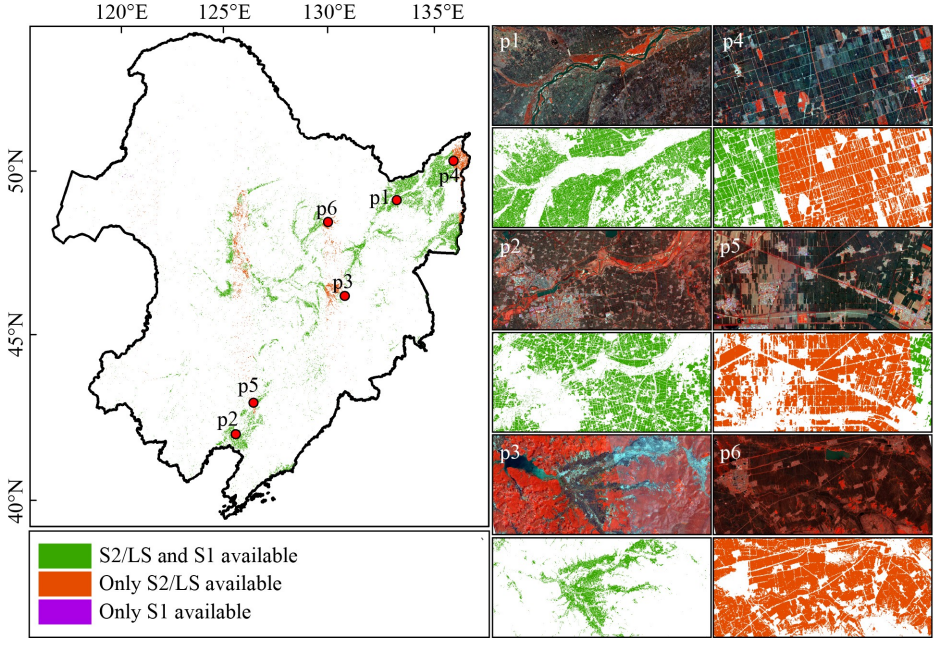

Fig. 8 Paddy rice distribution under different image availability. p1−p3 present zoom-in views of typical areas and their Sentinel-2 standard false color composite images (p1) along Songhua River, (p2) along Liao River, and (p3) in the mountainous region. p4−p6 are zoom-in views of paddy rice identification results when only optical images are available.

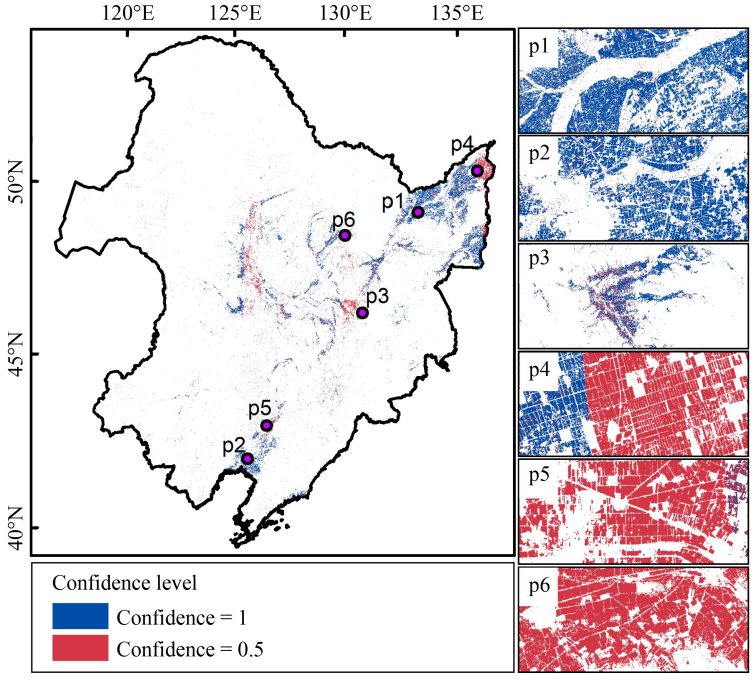

Fig. 9 Paddy rice distribution at different confidence levels. p1–p6 are zoom-in views of the paddy rice confidence map at locations corresponding to the paddy rice identification results in Fig. 8.

images in some areas with $N_{opt} > 0$ and $N_{SAR} > 1$ during the flooding stage (see Discussion section for more detail). At the municipal level ($N = 40$), paddy rice areas estimated from our data set had an ME of 0.27×10^3 km^2 and RMSE of 0.52×10^3 km^2 when compared with You et al.'s (2021) study. Similarly, they had ME of 0.21×10^3 km^2 and RMSE of 0.31×10^3 km^2 when compared with Statistical Yearbook. There were significant linear relationships between the estimated rice areas from our data set with the areas of You et al.'s (2021) study (slope = 1.21, R^2 = 0.99) and Statistical Yearbooks (slope = 1.10, R^2 = 0.99) (Fig. 10(b)). The high agreement between the rice area at both the provincial and municipal levels derived from our study and the data from other data sets illustrates the reliability of our proposed algorithm and the resultant paddy rice map.

4 Discussion

4.1 Potential of the proposed paddy rice mapping algorithm

Accurate rice identification in areas where rice and wetland coexist, such as northeast China, has been a challenge due to their similar flooding characteristic (Jin et al., 2016). Here, we proposed an enhanced knowledge-based algorithm that combined time series S2, LS, and S1 images to enhance the accuracy of paddy rice maps in rice-wetland coexistent areas. The consistency between our rice area and national statistics (Fig. 10) proves the reliability of our paddy rice mapping algorithms and maps. In previous studies (Xiao et al., 2006; Dong et al., 2016b; Zhang et al., 2020), it was relatively easy to eliminate the impact of upland vegetation on paddy rice mapping by the unique flooding/transplanting feature of paddy rice. However, wetlands can exhibit temporal optical profiles similar to those of paddy rice (Zhou et al., 2016). In this study, we focused exclusively on the flooding stage of rice, instead of flooding/transplanting together, and updated the criteria for flooding signal identification from (LSWI > NDVI or LSWI > EVI) to [(LSWI > NDVI or LSWI > EVI) and (LSWI > 0.3)]. This threshold for LSWI (> 0.3) helps remove the impact of wetlands and better captures the open water signals of rice during the flooding phase.

Our method highlights the potential of combining time series S1 SAR polarization bands to improve rice identification accuracy, enabling a more comprehensive insight into the distinctions in physical structure and moisture characteristics between paddy rice and wetlands. Their different scattering mechanisms result in varied trends or degrees of change in backscattering values for paddy rice and wetlands during the flooding stage (Figs. 6(a) and 6(b)). Specifically, paddy rice exhibits significant downward trends and values falling below specific thresholds in both VV and VH channels during the flooding phase, whereas this was not the case for wetlands. The sharp drops of backscattering values in paddy rice have been recognized and applied in previous rice mapping studies (Singha et al., 2019; Zhan et al., 2021). Nevertheless, those studies focused only on VH band. In contrast, we found that wetlands also experienced a drop in VH during the stage when a

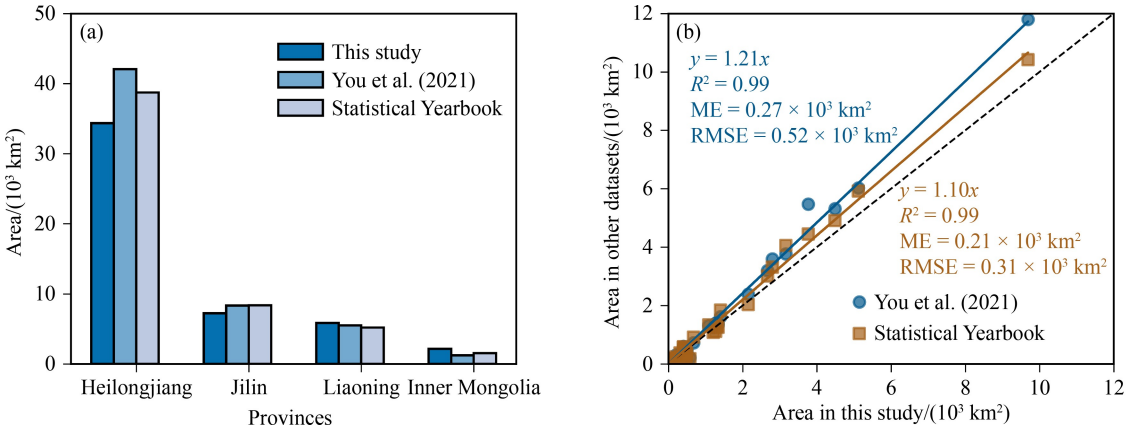

Fig. 10 Comparison of rice area estimated by our map and other data sets at (a) provincial and (b) municipal levels.

mixture of open water and dead plants and soils was presented (Fig. 6(b)). Interestingly, the difference in backscatter behavior between wetlands and paddy rice was more pronounced in the VV polarized channel than in the VH channel. During the flooding phase, VV values increased in wetlands but decreased in paddy rice (Fig. 6(a)). Therefore, the potential of incorporating VV in paddy rice identification is also worthy of attention and further investigation.

4.2 Potential sources of error in paddy rice maps

Integration of time series S2 and LS7/8 images in this study has increased the availability of high-quality optical observations compared to studies using only LS or S2 data. However, some pixels still have a limited number of high-quality observations during the flooding/transplanting period spanning from TGS-5-S to DOY 181d (Fig. 2(b)), which may lead to the failure to capture flooding/transplanting signals if all these observations were obtained in the later part of the flooding/transplanting period. In addition, some bad-quality observations in LS and S2 imagery due to cloud cover and cloud shadows may remain after employing quality filtering due to the inherent limitations of Cloud Probability and Quality Assessment bands (Zhu and Woodcock, 2012; Zou et al., 2018), which may result in low-frequency flood noise across and introduce uncertainties in the resultant maps. To further increase the number of high-quality observations, optical images with spatial resolution comparable to that of Sentinel-2 images, such as Worldview-3, could be integrated (Chen et al., 2019; Xian et al., 2019).

Numbers of S1 images may also affect rice map accuracy. Insufficient S1 observations during the flooding/transplanting period may cause failure to detect flooding/transplanting signals in paddy fields. Figure 11 shows an example of an underestimated paddy rice area in Qiqihar, Heilongjiang Province. S2 and LS7/8 time series data clearly demonstrated the presence of flooding signals during the period of TGS-5-S to DOY 181d (Fig. 11(e)). S1 time series data only comprised two observations: one at the beginning of the period when paddy field was covered with bare soil, and another at the end of the period when NDVI and EVI values had exceeded LSWI values, indicating rice canopy closure (Fig. 11(f)). Because of the limited number of S1 observations, S1 data could not capture flooding/transplanting events in this pixel (Figs. 11(d) and 11(f)). In further studies, SAR missions providing C-band imagery, such as RADARSAT-2 and the newer RADARSAT Constellation Mission (RCM), could be combined to overcome the constraints posed by limited S1 observations in certain areas.

4.3 Implications of the proposed paddy rice mapping algorithm and resultant map

With the increase in spatial and temporal resolution of remote sensing imagery, the need for more accurate and finer classifications becomes more critical (Fisher et al., 2018). Our analysis and proposed algorithm deepen our understanding of the spectral and structural features of paddy rice at different crop calendar phases by integrating optical, microwave, and thermal images, providing new insights and tools for mapping paddy rice in regions with similar climates without the need to collect a large amount of training samples (Dong et al., 2015; Zhang et al., 2023a). As the phenology of paddy rice and natural wetlands are consistent in normal years, our proposed paddy rice mapping algorithm can be directly applied in other years. The resultant 10-m paddy rice map advances our understanding of the area and spatial distribution of paddy rice in northeast China and provides important information and data support for rice cultivation planning and irrigation, carbon estimates, and food security. In addition, the proposed knowledge-based paddy rice algorithm has the potential to be transferred to other temperate regions where paddy rice is cultivated as single cropping system, such as the Yellow River Delta (Huang and Zhang, 2023), Japan (Inoue et al., 2020), and Korea Peninsula (Jo et al., 2020). However, careful study on

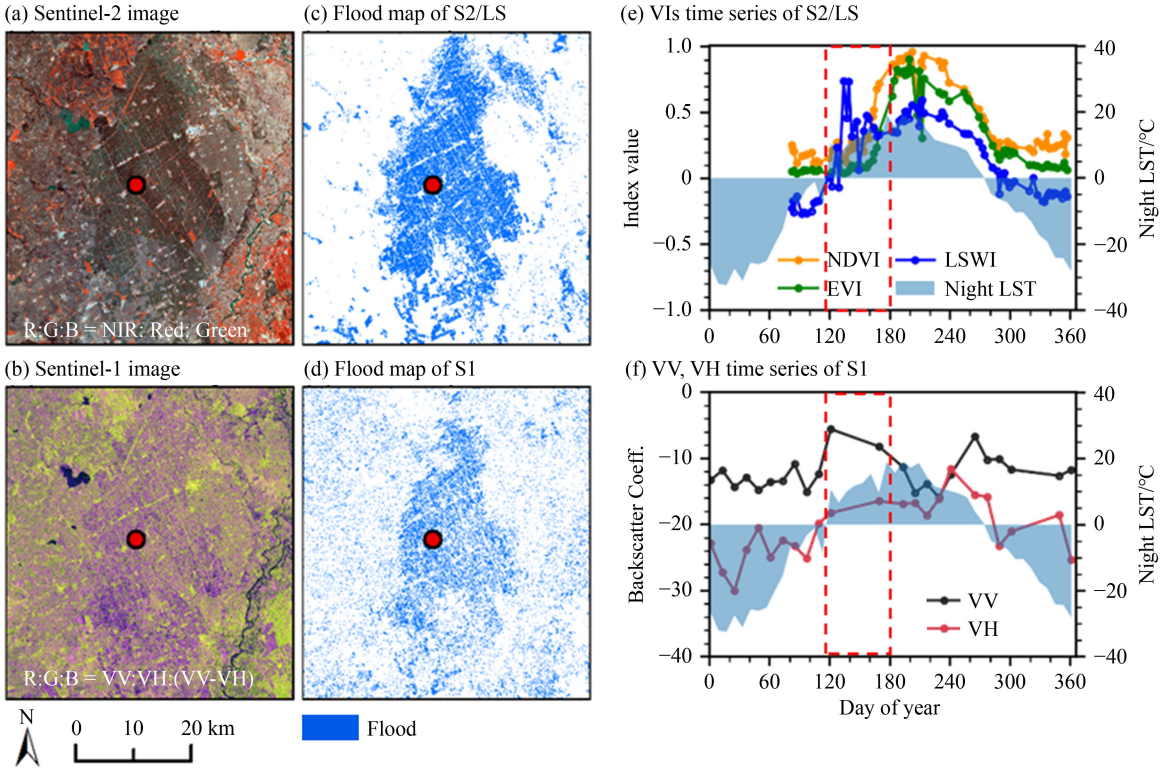

Fig. 11 Underestimated rice blocks in Qiqihar. (a–b) False color combinations of (a) Sentinel-2 mean and (b) Sentinel-1 mean from May 1 to June 30, 2023; (c–d) Flood maps derived from (c) Sentinle-2 and Landsat and (d) Sentinel-1 during the flooding stage; (e–f) Time series of (e) vegetation indices and (f) VV and VH for the red point (124.1413°E, 48.1804°N) in (a)–(d). Red hollow rectangles indicate the flooding period where images were used to identify flooding signals.

paddy rice cultivation practices (e.g., transplanting of rice seedlings) will be needed to ensure that they are the same as those in northeast China.

There were ~4.7% (3.32×10^7 pixels) of all the paddy rice pixels where flooding signals were detected by both optical and SAR images on the same date ($Flood_{opt}(t) = 1$ and $Flood_{SAR}(t) = 1$). This subset of data can serve as a large number of pure paddy rice training samples for information-based supervised classification using machine learning or deep learning algorithms. Many information-based classification approaches require a large amount of training data to build effective models (You et al., 2021; Gilić et al., 2023). However, prevailing training sample collection methods mainly rely on fieldwork or manual interpretation of high or very high spatial resolution images, which are both time- and labor-consuming, especially for large-scale land cover mapping (Ghorbanian et al., 2020; Gilić et al., 2023). In future studies, it would be meaningful and efficient to combine knowledge-based and information-based algorithms to overcome the limitations of image scarcity during the flooding/transplanting stages in knowledge-based algorithms, and the constraints imposed by the availability of training samples in information-based algorithms (Zhang et al., 2023b). Specifically, knowledge-based algorithms allow for the automatic generation of training samples for data-based classifiers, which can then utilize these samples along with all available remote sensing data throughout the year for paddy rice mapping.

5 Conclusions

The current optical image-based paddy rice algorithms face a series of challenges, including data quality issues (e.g., rainfall and clouds) and similar spectral characteristics with other water-related land cover (i.e., natural wetlands), which result in failure in flooding detection and introduction commission errors in paddy rice identification. In this study, we developed an enhanced knowledge-based paddy rice mapping algorithm by combining time series optical (Sentinel-2, Landsat7/8), microwave (Sentinel-1), and thermal (MODIS) images to overcome these issues. We generated a paddy rice map and a confidence level map using our proposed algorithms in northeast China at 10-m spatial resolution for 2020. The resultant paddy rice map had high accuracy with overall, producer's, and user's accuracies, and F1-score of 0.984 ± 0.001, 0.741 ± 0.010, 0.908 ± 0.004, and 0.816, respectively, which indicated the effectiveness and reliability of the proposed algorithms. There were $60.83 \pm 0.86 \times 10^3$ km^2 of paddy rice in northeast China in 2020, and most of them were

cultivated along rivers in plains with flat terrain and abundant water resources. The estimated provincial and municipal rice areas were highly consistent with data from other data set and the Statistical Yearbooks. Among the identified paddy rice pixels, 62.0% had a confidence level of 1, while 38.0% had a confidence level of 0.5. This study demonstrates the potential of combining time-series optical and microwave images to accurately identify paddy rice over a large spatial domain, and our paddy rice map can provide vital spatial and area information for paddy rice management and planning in northeast China.

Electronic Supplementary material is available in the online version of this article at http://dx.doi.org/10.1007/s11707-025-1154-1 and is accessible for authorized users.

Acknowledgments This study was in part supported by grants from the US National Science Foundation (Nos. 1911955, 2200310), the National Key Research and Development Program of China (No. 2023YFF0806900), and the China Postdoctoral Science Foundation (Nos. 2021TQ0072, 2021M700835). We thank the editors and reviewers for their time and effort in the review of our manuscript, and their comments and suggestions helped us to improve the manuscript.

Competing interests The authors declare that they have no competing interests.

References

Brisco B (2015). Mapping and monitoring surface water and wetlands with synthetic aperture radar. Remote Sensing of Wetlands: Applications and Advances, 119–136

Brisco B, Short N, Sanden J, Landry R, Raymond D (2009). A semi-automated tool for surface water mapping with RADARSAT-1. Can J Rem Sens, 35(4): 336–344

Chandrasekar K, Sesha Sai M, Roy P, Dwevedi R (2010). Land Surface Water Index (LSWI) response to rainfall and NDVI using the MODIS Vegetation Index product. Int J Remote Sens, 31(15): 3987–4005

Chen W, Li X, Wang L (2019). Fine land cover classification in an open pit mining area using optimized support vector machine and worldview-3 imagery. Remote Sens (Basel), 12(1): 82

Dong J, Xiao X (2016). Evolution of regional to global paddy rice mapping methods: a review. ISPRS J Photogramm Remote Sens, 119: 214–227

Dong J, Xiao X, Kou W, Qin Y, Zhang G, Li L, Jin C, Zhou Y, Wang J, Biradar C, Liu J, Moore B III (2015). Tracking the dynamics of paddy rice planting area in 1986–2010 through time series Landsat images and phenology-based algorithms. Remote Sens Environ, 160: 99–113

Dong J, Xiao X, Menarguez M A, Zhang G, Qin Y, Thau D, Biradar C, Moore B III (2016a). Mapping paddy rice planting area in northeastern Asia with Landsat 8 images, phenology-based algorithm and Google Earth Engine. Remote Sens Environ, 185: 142–154

Dong J, Xiao X, Zhang G, Menarguez M, Choi C, Qin Y, Luo P, Zhang Y, Moore B (2016b). Northward expansion of paddy rice in northeastern Asia during 2000–2014. Geophys Res Lett, 43(8): 3754–3761

Elliott J, Deryng D, Müller C, Frieler K, Konzmann M, Gerten D, Glotter M, Flörke M, Wada Y, Best N, Eisner S, Fekete B M, Folberth C, Foster I, Gosling S N, Haddeland I, Khabarov N, Ludwig F, Masaki Y, Olin S, Rosenzweig C, Ruane A C, Satoh Y, Schmid E, Stacke T, Tang Q, Wisser D (2014). Constraints and potentials of future irrigation water availability on agricultural production under climate change. Proc Natl Acad Sci USA, 111(9): 3239–3244

FAOSTAT (2020). Statistical database of the food and agricultural organization of the United Nations

Fisher J R, Acosta E A, Dennedy-Frank P J, Kroeger T, Boucher T M (2018). Impact of satellite imagery spatial resolution on land use classification accuracy and modeled water quality. Remote Sens Ecol Conserv, 4(2): 137–149

Geudtner D, Torres R, Snoeij P, Davidson M, Rommen B (2014). Sentinel-1 system capabilities and applications. In: 2014 IEEE Geoscience and Remote Sensing Symposium. IEEE, 1457–1460

Ghorbanian A, Kakooei M, Amani M, Mahdavi S, Mohammadzadeh A, Hasanlou M (2020). Improved land cover map of Iran using Sentinel imagery within Google Earth Engine and a novel automatic workflow for land cover classification using migrated training samples. ISPRS J Photogramm Remote Sens, 167: 276–288

Gilbert M, Golding N, Zhou H, Wint G, Robinson T P, Tatem A J, Lai S, Zhou S, Jiang H, Guo D, Huang Z, Messina J P, Xiao X, Linard C, Van Boeckel T P, Martin V, Bhatt S, Gething P W, Farrar J J, Hay S I, Yu H (2014). Predicting the risk of avian influenza A H7N9 infection in live-poultry markets across Asia. Nat Commun, 5(1): 4116

Gilić F, Gašparović M, Baučić M (2023). Current state and challenges in producing large-scale land cover maps: review based on recent land cover products. Geocarto Int, 38(1): 2242693

Gómez C, White J C, Wulder M A (2016). Optical remotely sensed time series data for land cover classification: a review. ISPRS J Photogramm Remote Sens, 116: 55–72

Guan X, Huang C, Liu G, Meng X, Liu Q (2016). Mapping rice cropping systems in Vietnam using an NDVI-based time-series similarity measurement based on DTW distance. Remote Sens (Basel), 8(1): 19

Guan X, Liu G, Huang C, Meng X, Liu Q, Wu C, Ablat X, Chen Z, Wang Q (2018). An open-boundary locally weighted dynamic time warping method for cropland mapping. ISPRS Int J Geoinf, 7(2): 75

Gumma M K, Nelson A, Thenkabail P S, Singh A N (2011). Mapping rice areas of South Asia using MODIS multitemporal data. J Appl Remote Sens, 5(1): 053547

Hall D K, Riggs G A, Salomonson V V (1995). Development of methods for mapping global snow cover using moderate resolution imaging spectroradiometer data. Remote Sens Environ, 54(2): 127–140

Huang C, Zhang C (2023). Time-series remote sensing of rice paddy expansion in the Yellow River Delta: towards sustainable ecological conservation in the context of water scarcity. Remote

Sens Ecol Conserv, 9(4): 454–468

Huang C, Zhang C, He Y, Liu Q, Li H, Su F, Liu G, Bridhikitti A (2020). Land cover mapping in cloud-prone tropical areas using Sentinel-2 data: integrating spectral features with NDVI temporal dynamics. Remote Sens (Basel), 12(7): 1163

Huete A, Didan K, Miura T, Rodriguez E P, Gao X, Ferreira L G (2002). Overview of the radiometric and biophysical performance of the MODIS vegetation indices. Remote Sens Environ, 83(1−2): 195–213

Huete A, Liu H, Batchily K, Van Leeuwen W (1997). A comparison of vegetation indices over a global set of TM images for EOS-MODIS. Remote Sens Environ, 59(3): 440–451

Inoue S, Ito A, Yonezawa C (2020). Mapping paddy fields in Japan by using a Sentinel-1 SAR time series supplemented by Sentinel-2 images on Google Earth Engine. Remote Sens (Basel), 12(10): 1622

Jin C, Xiao X, Dong J, Qin Y, Wang Z (2016). Mapping paddy rice distribution using multi-temporal Landsat imagery in the Sanjiang Plain, northeast China. Front Earth Sci, 10(1): 49–62

Jo H W, Lee S, Park E, Lim C H, Song C, Lee H, Ko Y, Cha S, Yoon H, Lee W K (2020). Deep learning applications on multitemporal SAR (Sentinel-1) image classification using confined labeled data: the case of detecting rice paddy in South Korea. IEEE Trans Geosci Remote Sens, 58(11): 7589–7601

Le Toan T, Ribbes F, Wang L F, Floury N, Ding K H, Kong J A, Fujita M, Kurosu T (1997). Rice crop mapping and monitoring using ERS-1 data based on experiment and modeling results. IEEE Trans Geosci Remote Sens, 35(1): 41–56

Li H, Fu D, Huang C, Su F, Liu Q, Liu G, Wu S (2020). An approach to high-resolution rice paddy mapping using time-series Sentinel-1 SAR data in the Mun River Basin, Thailand. Remote Sens (Basel), 12(23): 3959

Liu J, Kuang W, Zhang Z, Xu X, Qin Y, Ning J, Zhou W, Zhang S, Li R, Yan C, Wu S, Shi X, Jiang N, Yu D, Pan X, Chi W (2014). Spatiotemporal characteristics, patterns, and causes of land-use changes in China since the late 1980s. J Geogr Sci, 24(2): 195–210

Liu L, Xiao X, Qin Y, Wang J, Xu X, Hu Y, Qiao Z (2020). Mapping cropping intensity in China using time series Landsat and Sentinel-2 images and Google Earth Engine. Remote Sens Environ, 239: 111624

Liu M, Li H, Li L, Man W, Jia M, Wang Z, Lu C (2017). Monitoring the invasion of Spartina alterniflora using multi-source high-resolution imagery in the Zhangjiang Estuary, China. Remote Sens (Basel), 9(6): 539

McNairn H, Jiao X, Pacheco A, Sinha A, Tan W, Li Y (2018). Estimating canola phenology using synthetic aperture radar. Remote Sens Environ, 219: 196–205

Nguyen T T H, De Bie C, Ali A, Smaling E, Chu T H (2012). Mapping the irrigated rice cropping patterns of the Mekong delta, Vietnam, through hyper-temporal SPOT NDVI image analysis. Int J Remote Sens, 33(2): 415–434

Ni R, Tian J, Li X, Yin D, Li J, Gong H, Zhang J, Zhu L, Wu D (2021). An enhanced pixel-based phenological feature for accurate paddy rice mapping with Sentinel-2 imagery in Google Earth Engine. ISPRS J Photogramm Remote Sens, 178: 282–296

Oguro Y, Suga Y, Takeuchi S, Ogawa M, Konishi T, Tsuchiya K (2001). Comparison of SAR and optical sensor data for monitoring of rice plant around Hiroshima. Adv Space Res, 28(1): 195–200

Olofsson P, Foody G M, Herold M, Stehman S V, Woodcock C E, Wulder M A (2014). Good practices for estimating area and assessing accuracy of land change. Remote Sens Environ, 148: 42–57

Pan X Z, Uchida S, Liang Y, Hirano A, Sun B (2010). Discriminating different landuse types by using multitemporal NDXI in a rice planting area. Int J Remote Sens, 31(3): 585–596

Panigrahy S, Parihar J (1992). Role of middle infrared bands of Landsat thematic mapper in determining the classification accuracy of rice. Int J Remote Sens, 13(15): 2943–2949

Parmuchi M G, Karszenbaum H, Kandus P (2002). Mapping wetlands using multi-temporal RADARSAT-1 data and a decision-based classifier. Can J Rem Sens, 28(2): 175–186

Qin Y, Xiao X, Dong J, Chen B, Liu F, Zhang G, Zhang Y, Wang J, Wu X (2017). Quantifying annual changes in built-up area in complex urban-rural landscapes from analyses of PALSAR and Landsat images. ISPRS J Photogramm Remote Sens, 124: 89–105

Qin Y, Xiao X, Dong J, Zhang G, Roy P S, Joshi P K, Gilani H, Murthy M S R, Jin C, Wang J, Zhang Y, Chen B, Menarguez M A, Biradar C M, Bajgain R, Li X, Dai S, Hou Y, Xin F, Moore B III (2016). Mapping forests in monsoon Asia with ALOS PALSAR 50-m mosaic images and MODIS imagery in 2010. Sci Rep, 6(1): 20880

Qin Y, Xiao X, Dong J, Zhang G, Shimada M, Liu J, Li C, Kou W, Moore B III (2015a). Forest cover maps of China in 2010 from multiple approaches and data sources: PALSAR, Landsat, MODIS, FRA, and NFI. ISPRS J Photogramm Remote Sens, 109: 1–16

Qin Y, Xiao X, Dong J, Zhou Y, Zhu Z, Zhang G, Du G, Jin C, Kou W, Wang J, Li X (2015b). Mapping paddy rice planting area in cold temperate climate region through analysis of time series Landsat 8 (OLI), Landsat 7 (ETM+) and MODIS imagery. ISPRS J Photogramm Remote Sens, 105: 220–233

Qin Y, Xiao X, Wigneron J P, Ciais P, Brandt M, Fan L, Li X, Crowell S, Wu X, Doughty R, Zhang Y, Liu F, Sitch S, Moore B III (2021). Carbon loss from forest degradation exceeds that from deforestation in the Brazilian Amazon. Nat Clim Chang, 11(5): 442–448

Rao P N, Rao V (1987). Rice crop identification and area estimation using remotely-sensed data from Indian cropping patterns. Int J Remote Sens, 8(4): 639–650

Shao Y, Fan X, Liu H, Xiao J, Ross S, Brisco B, Brown R, Staples G (2001). Rice monitoring and production estimation using multitemporal RADARSAT. Remote Sens Environ, 76(3): 310–325

Singha M, Dong J, Zhang G, Xiao X (2019). High resolution paddy rice maps in cloud-prone Bangladesh and Northeast India using Sentinel-1 data. Sci Data, 6(1): 26

Tollefson J (2022). Scientists raise alarm over'dangerously fast'growth in atmospheric methane. Nature,doi: 10.1038/d41586-022-00312-2

Torres R, Snoeij P, Geudtner D, Bibby D, Davidson M, Attema E, Potin P, Rommen B, Floury N, Brown M, Traver I N, Deghaye P, Duesmann B, Rosich B, Miranda N, Bruno C, L'Abbate M, Croci R, Pietropaolo A, Huchler M, Rostan F (2012). GMES Sentinel-1 mission. Remote Sens Environ, 120: 9–24

Tucker C J (1979). Red and photographic infrared linear combinations

for monitoring vegetation. Remote Sens Environ, 8(2): 127–150

Turker M, Ozdarici A (2011). Field-based crop classification using SPOT4, SPOT5, IKONOS and QuickBird imagery for agricultural areas: a comparison study. Int J Remote Sens, 32(24): 9735–9768

Wan Z (2008). New refinements and validation of the MODIS land-surface temperature/emissivity products. Remote Sens Environ, 112(1): 59–74

Wang J, Xiao X, Qin Y, Dong J, Zhang G, Kou W, Jin C, Zhou Y, Zhang Y (2015). Mapping paddy rice planting area in wheat-rice double-cropped areas through integration of Landsat-8 OLI, MODIS and PALSAR images. Sci Rep, 5(1): 10088

Wang X, Xiao X, Zou Z, Dong J, Qin Y, Doughty R B, Menarguez M A, Chen B, Wang J, Ye H, Ma J, Zhong Q, Zhao B, Li B (2020a). Gainers and losers of surface and terrestrial water resources in China during 1989–2016. Nat Commun, 11(1): 3471

Wang X, Xiao X, Zou Z, Hou L, Qin Y, Dong J, Doughty R B, Chen B, Zhang X, Chen Y, Ma J, Zhao B, Li B (2020b). Mapping coastal wetlands of China using time series Landsat images in 2018 and Google Earth Engine. ISPRS J Photogramm Remote Sens, 163: 312–326

Xian G, Shi H, Dewitz J, Wu Z (2019). Performances of WorldView 3, Sentinel 2, and Landsat 8 data in mapping impervious surface. Remote Sens Appl Soc Environ, 15: 100246

Xiao X, Boles S, Frolking S, Li C, Babu J Y, Salas W, Moore B III (2006). Mapping paddy rice agriculture in South and Southeast Asia using multi-temporal MODIS images. Remote Sens Environ, 100(1): 95–113

Xiao X, Boles S, Frolking S, Salas W, Moore B III, Li C, He L, Zhao R (2002a). Observation of flooding and rice transplanting of paddy rice fields at the site to landscape scales in China using VEGETATION sensor data. Int J Remote Sens, 23(15): 3009–3022

Xiao X, Boles S, Liu J, Zhuang D, Frolking S, Li C, Salas W, Moore B III (2005a). Mapping paddy rice agriculture in southern China using multi-temporal MODIS images. Remote Sens Environ, 95(4): 480–492

Xiao X, He L, Salas W, Li C, Moore B III, Zhao R, Frolking S, Boles S (2002b). Quantitative relationships between field-measured leaf area index and vegetation index derived from VEGETATION images for paddy rice fields. Int J Remote Sens, 23(18): 3595–3604

Xiao X, Hollinger D, Aber J, Goltz M, Davidson E A, Zhang Q, Moore B III (2004). Satellite-based modeling of gross primary production in an evergreen needleleaf forest. Remote Sens Environ, 89(4): 519–534

Xiao X, Zhang Q, Hollinger D, Aber J, Moore B III (2005b). Modeling gross primary production of an evergreen needleleaf forest using MODIS and climate data. Ecol Appl, 15(3): 954–969

Yan C, Li Z, Zhang Z, Sun Y, Wang Y, Xin Q (2023). High-resolution mapping of paddy rice fields from unmanned airborne vehicle images using enhanced-TransUnet. Comput Electron Agric, 210: 107867

You N, Dong J, Huang J, Du G, Zhang G, He Y, Yang T, Di Y, Xiao X (2021). The 10-m crop type maps in northeast China during 2017–2019. Sci Data, 8(1): 41

Zhan P, Zhu W, Li N (2021). An automated rice mapping method based on flooding signals in synthetic aperture radar time series. Remote Sens Environ, 252: 112112

Zhang C, Xiao X, Wang X, Qin Y, Doughty R, Yang X, Meng C, Yao Y, Dong J (2024). Mapping wetlands in northeast China by using knowledge-based algorithms and microwave (PALSAR-2, Sentinel-1), optical (Sentinel-2, Landsat), and thermal (MODIS) images. J Environ Manage, 349: 119618

Zhang C, Xiao X, Zhao L, Qin Y, Doughty R, Wang X, Dong J, Yang X (2023a). Mapping Eucalyptus plantation in Guangxi, China by using knowledge-based algorithms and PALSAR-2, Sentinel-2, and Landsat images in 2020. Int J Appl Earth Obs Geoinf, 120: 103348

Zhang C, Zhang H, Tian S (2023b). Phenology-assisted supervised paddy rice mapping with the Landsat imagery on Google Earth Engine: experiments in Heilongjiang Province of China from 1990 to 2020. Comput Electron Agric, 212: 108105

Zhang G, Xiao X, Biradar C M, Dong J, Qin Y, Menarguez M A, Zhou Y, Zhang Y, Jin C, Wang J, Doughty R B, Ding M, Moore B III (2017). Spatiotemporal patterns of paddy rice croplands in China and India from 2000 to 2015. Sci Total Environ, 579: 82–92

Zhang G, Xiao X, Dong J, Kou W, Jin C, Qin Y, Zhou Y, Wang J, Menarguez M A, Biradar C (2015). Mapping paddy rice planting areas through time series analysis of MODIS land surface temperature and vegetation index data. ISPRS J Photogramm Remote Sens, 106: 157–171

Zhang G, Xiao X, Dong J, Xin F, Zhang Y, Qin Y, Doughty R B, Moore B III (2020). Fingerprint of rice paddies in spatial–temporal dynamics of atmospheric methane concentration in monsoon Asia. Nat Commun, 11(1): 554

Zhou Y, Xiao X, Qin Y, Dong J, Zhang G, Kou W, Jin C, Wang J, Li X (2016). Mapping paddy rice planting area in rice-wetland coexistent areas through analysis of Landsat 8 OLI and MODIS images. Int J Appl Earth Obs Geoinf, 46: 1–12

Zhu Z, Woodcock C E (2012). Object-based cloud and cloud shadow detection in Landsat imagery. Remote Sens Environ, 118: 83–94

Zou Z, Xiao X, Dong J, Qin Y, Doughty R B, Menarguez M A, Zhang G, Wang J (2018). Divergent trends of open-surface water body area in the contiguous United States from 1984 to 2016. Proc Natl Acad Sci USA, 115(15): 3810–3815